



PII: S0010-4825(97)00023-1

ALGORITHM FOR PURKINJE IMAGES I AND IV AND LIMBUS CENTRE LOCALIZATION

J.C. BARRY^a, U.M. PONGS^a and W. HILLEN^b

^a Department of Ophthalmology, Aachen University Hospital RWTH, Pauwelsstr. 30, D-52057 Aachen, Germany

^b Department of Engineering, Fachhochschule Aachen, Abt. Jülich, Ginsterweg 1, D-52428 Jülich, Germany

(Received 1 October 1996; revised 9 May 1997)

Abstract—Purpose: To develop a fast and reliable image processing algorithm for the extraction of Purkinje reflection data for measurement of ocular alignment with standard PC hardware.

Methods: Purkinje images I and IV are specular reflections of light sources, the positions of which are proportional to eye rotation. Fast histogram-based thresholding and gradient techniques were used to localize Purkinje images I and IV, the pupil centre and the limbus centre in images obtained with near infrared light.

Results and Conclusions: Execution time was 500 ms per eye. A set of 540 images was evaluated of which 94% were automatically analysed. © 1997 Elsevier Science Ltd.

Ophthalmology	Ocular alignment	Strabismus	Image processing
Screening	Purkinje image	Pupil center	Limbus center
diagnosis	Infrared light	Purkinje I and IV reflection pattern evaluation	Automated

1. INTRODUCTION

1.1. Clinical background

We are interested in the development of screening techniques for *ocular misalignment* in infants under natural viewing conditions. Ocular misalignment and refractive errors, if not treated in the first years of life, may lead to irreversible developmental visual impairment, or amblyopia [1,2]. In most cases, this results in lifelong loss of reading ability in the affected eye.

By contrast, early treatment of amblyopia with glasses and patching is simple and cost-effective. However, since infants, toddlers and children are not aware of the visual deficiency they are subject to, and since this condition may not be noticed by the parents or non-specialized examiners, early screening is necessary. To improve early treatment [3,4] of visual impairment in the critical period up to school age, techniques for the detection of microtropia are needed [5]. Microtropia [2], a small, cosmetically non-conspicuous ocular misalignment from fractions of a degree to 5°, is one risk factor for amblyopia. Most promising for large scale, cost effective, automated, objective ocular misalignment screening are techniques that evaluate digitized images of the anterior eye segment and Purkinje images [6].

1.2. Ocular alignment measurement with Purkinje reflexes

In vision sciences, specular images of the anterior segment of the eye are named *Purkinje images* [7] after the physiologist J. E. Purkinje who described them first [8]. Specular reflection from the optical interfaces of the anterior eye segment gives rise to a series of images or reflexes, from the anterior (Purkinje image I) and posterior (Purkinje image II) corneal surfaces and from the anterior (Purkinje image III) and posterior (Purkinje image IV) crystalline lens surfaces. Their position or shift is approximately proportional to an

*Author to whom correspondence should be addressed

eye's rotation angle. Clinically, Purkinje images have long been used to examine ocular misalignment, going back to the corneal reflex method first described by Hirschberg [9].

Many techniques have been described for ocular alignment measurement. Some achieve a high accuracy through the use of bite bars, chin/head rests, or by using special goggles or glasses. From a screening point of view, techniques are only of interest if they are well tolerated by infants and maintain natural viewing conditions.

Some screening techniques use the position of the corneal reflex relative to the eye's anterior segment as a measurement parameter. The corneal reflex is the specular image of an object or light source in front of the eyes.

In essence, all corneal reflex techniques use the distance or shift, x , of the corneal reflex from a reference point, usually the pupil centre, to assess the ocular alignment. The distance, x , of Purkinje image I (measured in mm) is proportional to the eye rotation ϕ for small values of x , where the approximation $\arcsin(x) \approx x$ [9] holds. In clinical testing, the examiner estimates the difference in the position of the corneal reflexes of the right and left eye in an adult or infant during a screening examination. Typically, a fixed, so-called Hirschberg ratio of about $12^\circ/\text{mm}$ (21–22 PD/mm) [10] is used, regardless of the eye's individual characteristics and age [11]. The limited accuracy of this clinical test led to the development of photographic or video techniques, where the position of Purkinje image I position is measured in mm following a calibration. Since Purkinje image I is a bright, easily retrieveable structure in an image, as soon as image processing became feasible with PCs, algorithms were developed for the localization of the corneal reflex, for instance, in digitized, binary images, with thresholding techniques [12,13].

In order to perform real time corneal reflex tracking signal processors had to be used to overcome the limited speed of standard PC hardware components. However, measurement accuracy with digital imaging devices is also limited by the calibration error, and the error linked to the use of the correct Hirschberg ratio, along with the error linked to the choice of the reference point for the measurement of the corneal reflex position. Usually the entrance *pupil centre* is chosen since the pupil offers a good contrast relative to the iris. The entrance pupil is the image of the pupil seen through the cornea; in the following, we will refer to the entrance pupil simply as the pupil. The pupil centre is determined by averaging the x and y coordinates of opposite outer pupil boundaries. However, the pupil centre position is easily biased through a rotated cornea, and asymmetric pupil constriction may lead to a pupil centre shift [14,15] without a corresponding eye rotation.

Therefore, measurement of the corneal reflex position is not sufficiently accurate for the detection of *small* ocular misalignments.

1.3. *Enhanced ocular alignment measurement with corneal and crystalline lens reflexes*

Purkinje image I and IV reflection pattern evaluation is a technique for the accurate measurement of ocular misalignment, using Purkinje images I and IV [16–18]. Figure 1 shows a digitized image of a left eye with three Purkinje images I (lower row of bright spots in the pupil) and three Purkinje images IV (upper row of small spots in the pupil). This ocular alignment technique offers advantages over other techniques that use the corneal reflection (Purkinje image 1) alone since it measures large and *small* ocular alignments accurately [19]. However, due to the nature of Purkinje image IV, image processing algorithms developed for the identification or tracking of the corneal reflex [12] are not appropriate.

In this paper we introduce a simple and fast algorithm for the localization of Purkinje images I and IV and the limbal centre in both eyes from digitized IR images of eyes, optimized for use with an automated ocular misalignment screening device.

2. SYSTEM AND METHODS

2.1. *Purkinje I and IV reflection pattern evaluation*

Purkinje I and IV reflection pattern evaluation uses the horizontal and vertical distances between Purkinje images I and IV, calculated as the differences between x and y coordinates

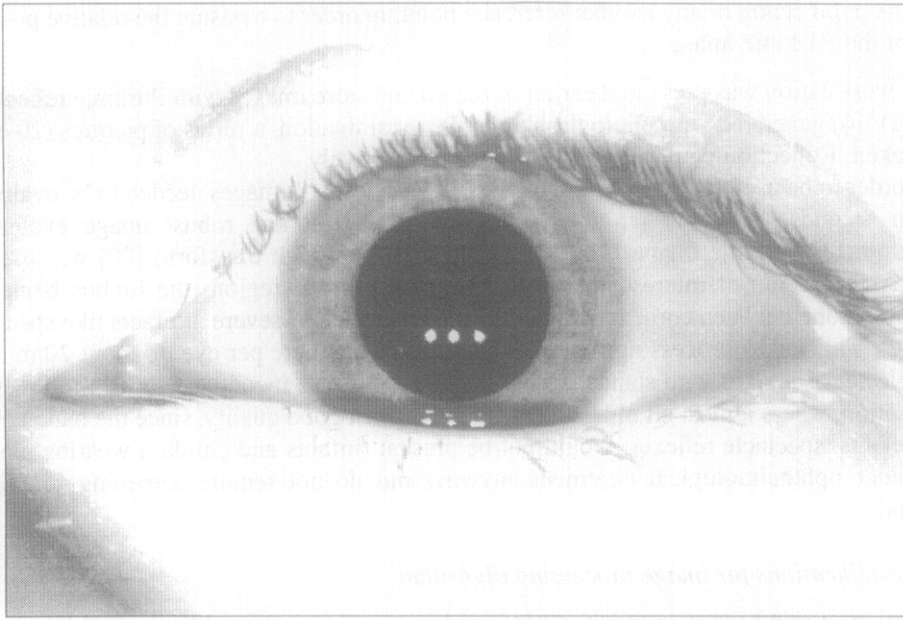


Fig. 1. Digitized image of a left eye with Purkinje I and IV reflection pattern.

of the images coordinates in the digitized pictures, see Fig. 1. The computation of the eye alignment from the Purkinje I and IV reflection's coordinates (see Figs 1 and 2) is done by means of formulae presented elsewhere [18] which are not relevant in the context of this paper. This *new* technique for ocular alignment measurement, offers the following advantages:

- no calibration is required, since only the *relative* distances between Purkinje images I and IV, measured in *arbitrary* units (for instance pixels) need to be known [19].
- no reference point is needed; that is the method does not require the determination of

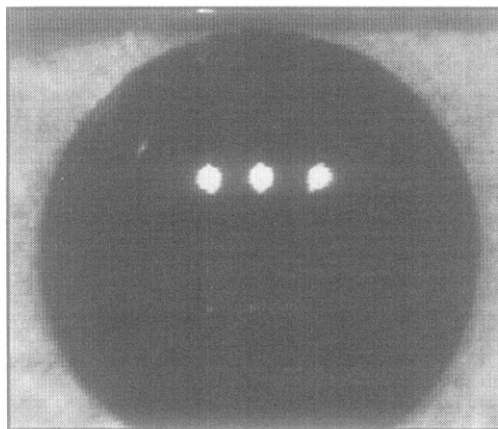


Fig. 2. Enlarged pupil region of Fig. 1. Three infrared light sources pointing at the eye from below the eye's visual axis were used for this picture. Note the larger, saturated lower row of reflections, the anterior corneal reflections (Purkinje image I), and the smaller, dimmer upper row of reflections, the posterior crystalline lens reflections (Purkinje images IV). To compute the eye's alignment, the coordinates of the centres of the Purkinje images must be localized, ruling out artifacts with similar grey levels or of similar size. These coordinates are used with known formulae that do not need to be known within the scope of this paper. The pupil boundary has a high contrast with the iris, whereas the boundary between the cornea and the sclera, the limbus, is less well defined. Also, note artefacts, like the three reflections from the tear film, close to the lower lid, that are as bright as the corneal reflections. Eyeglasses may be the cause of additional artifacts. Finally, note reflections of the nose and of the eyelashes visible against the dark pupillary background.

the pupil centre or any another reference point, in order to measure the relative position of the Purkinje image.

A PC workstation was presented earlier to record and store images with Purkinje reflections I and IV [6] generated with photo flash units. Per examination, a series of pictures (20 eyes) was taken. Reflection patterns were evaluated interactively.

In order to be used routinely as a screening device, a set of images needed to be evaluated within seconds. In an earlier attempt to develop a fast and robust image evaluation algorithm for Purkinje image I and IV localization, a Hough transform [20] was used to identify the region of interest, that is the pupil and limbal region (the limbus being the transition zone between cornea and sclera) in the presence of severe artefacts like spectacle reflexes. This led to processing times of the order of a minute per eye or about 20 min for a whole set of images with standard PC hardware. This was incompatible with a screening application, where almost all image data were of at least good quality, since the main source of artefacts, spectacle reflexes, would not be present (infants and children wearing glasses are under ophthalmological treatment anyway, and do not require screening for visual defects).

2.2. Specifications for image processing algorithm

Bearing in mind the prerequisites addressed above, a fast algorithm for Purkinje image I and IV localization in images taken without glasses, should be developed, which did not require costly special hardware like signal processors. On the contrary, image processing time should be reduced by using simple algorithms, and by making the best use of the processing speed available with *standard* CPUs and framegrabbers.

Images deteriorated by artefacts (other than spectacle artefacts) should be identified by the algorithm in order to guarantee diagnostic safety. Artefacts impairing image quality could result from altered tear film or inflamed conjunctiva, corneal scarring, crystalline lens opacifications, ptosis (drooping of the upper eyelid) and other *pathological conditions* which require a referral. These image data should be identified reliably.

Images that could not be evaluated properly due to *technical imperfection* (positions of eyelids and eyelashes, hair hanging in front of an eye and other) should be discarded. In these cases the algorithm must issue a warning so that images may be repeated.

Since the posterior crystalline lens image (Purkinje image IV) may not be observable in some cases due to corneal or lens opacification, or due to a *vertical misalignment* leading to a superimposition of Purkinje images, the algorithm should also be able to evaluate images where only Purkinje image I position is clearly retrievable. In this case the *absolute* Purkinje image position in millimeters relative to the *limbal centre* should be evaluated as an alternative to Purkinje I and IV reflection pattern evaluation. The use of the *limbus* centre for ocular misalignment measurement is less prone to systematic errors than that of the *pupil* centre (see Introduction), but its localization with image processing is more challenging.

To meet the requirements addressed above, the hardware was optimized and the development of the algorithm was done in three steps:

1. basic descriptive image analysis;
2. designing and testing software modules with a macro programming tool and using standard image processing software tools;
3. optimization of algorithm's speed in a higher programming language.

2.3. Hardware requirements

The choice of the system components directly affected the image quality. In order to keep the image processing algorithm simple and fast, the image signals to be processed had to be high in contrast, with few artefacts. The optimized hardware components included a pulsed array of three light sources to generate Purkinje I and IV reflection patterns (see Fig. 1) and two infrared sensitive CCD cameras (KP-160S, Hitachi Denshi Europe, Rodgau, Germany),

one for each eye, with adjusted, fixed gain. Lenses were chosen so that each eye would be imaged with a field of about 4 cm width by 3 cm height at 50 cm distance. The best results were obtained with three IREDs (OD50L, Ortel, Eching, Germany), $\lambda_{\text{peak}} = 880$ nm, separated by 8.8 cm from each other, illuminating the eyes from a distance of 50 cm, and 10–15 cm below the visual axes of the eyes. This equaled an angular subtense of the light sources of 10° . This set-up typically yielded a darker pupil compared with visible light images, increasing the contrast between the Purkinje images, which were located in or near the pupil region. Also, the limbal region showed improved contrast with infrared lighting compared to visible light illumination. The total radiance at the cornea was within the allowed exposure limits for near infrared light [21].

The images were digitized with two frame grabbers (LG3, Scion Corp., Frederick, MD, U.S.A.) and stored on an Apple Macintosh PC (7100 Power PC, Cupertino, CA, U.S.A.) with a 2nd level cache 256 kB, 66 MHz, 20 MB RAM. Image acquisition and handling in step 1 and 2 was done with NIH Image 1.57 public domain software [22].

3. ALGORITHM AND IMPLEMENTATION

3.1. Step 1—image characteristics

The resulting images had 768 by 512 pixels with 8bit depth, equaling 350 kB in storage size (see Fig. 1). The anterior segment of the eye was divided into several regions of interest for the basic descriptive image analysis, which was carried out on a representative image data base.

The darkest segment was the pupil segment. In it the two rows of Purkinje images I and IV could be found. Occasionally, Purkinje images fell outside this area, when fixation was not central. Also, Purkinje image III could accidentally be imaged in the pupil region. Purkinje image III is much larger than Purkinje image I, typically 2 to 3 times the diameter, and its average grey level was between that of Purkinje image I and of the pupil segment. This meant that it could add to the pupil's noise and had to be treated as an artefact. Again, this could happen in rare cases with a large ocular misalignment, when fixation was not central, or when there was sufficient internal ocular surface misalignment [23].

The pupil boundary had sharp contrast and was elliptical to circular in shape. The transition zone to the iris segment was very narrow, with a steep grey level discontinuity. The circular iris was somewhat lighter and, due to its mostly radially striated structure, less uniform than the pupil segment. Interestingly, the grey levels of light and dark irises were not systematically different under IR illumination, so that iris colour hardly contributed to iris grey level variation. The circular or elliptical transition zone from the transparent cornea to the white sclera is known as the limbal region. This roughly coincides with the outer iris boundary. The limbus, or corneal diameter (typically 11 mm diameter in an adult) would be about 60 pixels wide with the hardware set-up as described above. The sclera was mostly white, with noise coming mainly from superficial conjunctival capillaries and reflection. Sclera and corneal or pupillary regions could be covered partly by upper and lower eyelids, thus occluding the limbal contour in its upper and lower portion. In some cases the upper or lower eyelid would even reach over the pupillary region. Reflections from the transparent conjunctiva would occasionally be seen in the image too. Reflections from the tear film meniscus were frequently present directly above the lower eyelid. They were usually at the saturation level. Inhomogeneities in the tear film itself could be present all over the anterior eye segment, and in particular projecting upon the pupillary region, where they created additional noise. Also, eyelashes and their reflections could overlap the corneal and even the pupillary region.

As an example, Fig. 2 shows the enlarged region of interest, the pupil region of the original image (Fig. 1), and Fig. 3 shows its grey-scale plot. Note the difference between the saturated Purkinje images I and the smaller, less bright Purkinje images IV and the noise in the pupil region. In the nasal portion of the pupillary region the specular image of the subject's nose may be distinguished. Its peak grey levels are of the order of Purkinje image IV. Only the three corneal reflection peaks may be clearly separated from the pupil region

and from the iris. Figure 4 shows a histogram of the eye in Fig. 1. The pupil region is clearly represented by the detached peak on the right, representing "dark" grey levels. In the Macintosh computer system, white is represented by a grey level of 0, and black by the grey level 255. In the imaging system used in step 1 and 2 of this study, however, the grey scale was limited to grey levels ranging from 20 to 239.

Figure 5a shows a grey scale profile through the Purkinje images I (bottom) from Fig. 2 and Fig. 5b a profile through the Purkinje images IV (top) from Fig. 2. These reflect typical contrasts between the relevant image signals; the Purkinje images, the pupil region, the iris and the sclera. A series of images representing the variation of image characteristics was analyzed for typical values and ranges of image data. Tables 1–6 summarize the relevant

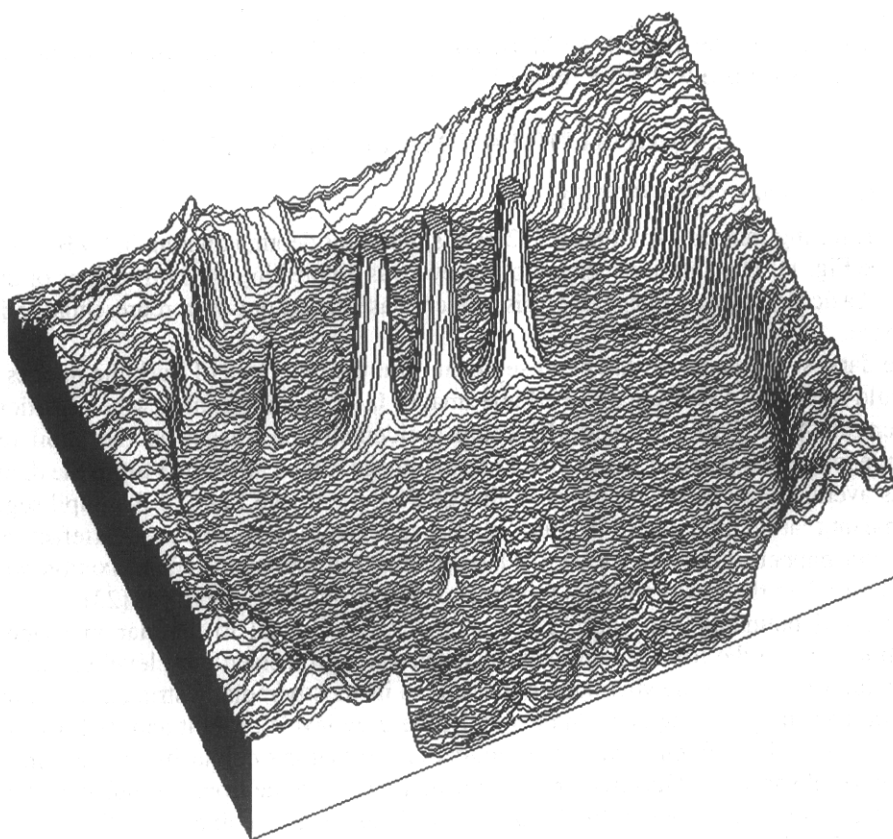


Fig. 3. A pseudo-3D greyscale plot of the pupil region (see Fig. 2) with artefacts. The plot has been rotated by 180° for better visibility.

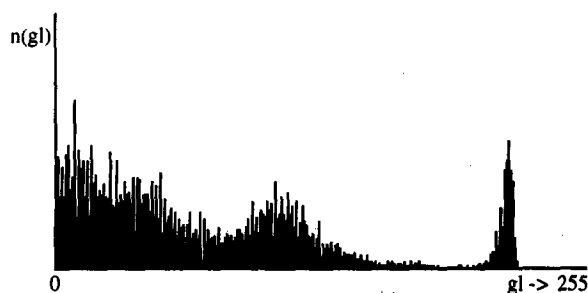


Fig. 4. Histogram (count n) of the unprocessed, original image shown in Fig. 1. Grey level (gi) 255 means black, 0 means white, due to Macintosh computer system idiosyncrasies. The peak in the upper grey scale region represents the dark pupil.

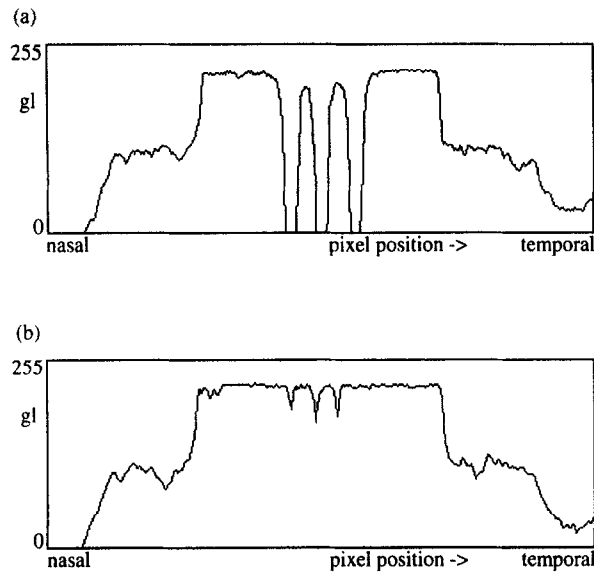


Fig. 5. (a) Greyscale profile through the row of Purkinje images I of Fig. 1. Grey level 255 means black, 0 means white. Therefore, the profile appears inverted compared to Fig. 3. Note the central pupil plateau, with three deep indentations from Purkinje images I. The grey levels fall off steeply at the boundary of the pupil with the iris. The iris region shows more noise than the pupil zone, and the transition from the iris to the white sclera is gentler and less well defined. The grey level slope of the limbal region is not intersected at its steepest locus, since the profile goes through the lower part of the pupil. (b) Greyscale profile through the row of Purkinje images IV of Fig. 1. The grey level height of Purkinje images IV is just higher than the typical noise in the pupil. Artefacts may have the same, or even lower grey levels than these images.

data that characterize Purkinje images I and IV, the pupil region and its outer boundary, the iris region, and the limbus transition zone.

The descriptive image analysis provided a knowledge base for the signals to be examined and extracted in the image processing. This *a priori* knowledge could be used—either to identify the Purkinje images and differentiate from artefactual structures or to perform a final check on the results reliability. Variations in the data are largely due to interindividual differences in pigmentation and ocular component size.

Artefacts arise, for instance, when reflections from the tear film reach the brightness and size of Purkinje images. Eyelashes or hair reaching in the pupil region may be reflected by

Tables 1–6: typical structures and their mean dimensions and ranges including slopes from a series of image data like Fig. 1. Hyphens (“—”) indicate values that either were not available or that were not relevant to the image characterization.

Table 1. Characteristic data of Purkinje images I and artefacts that resemble Purkinje images I. The form factor is the ratio of horizontal and vertical diameter

	Minimum	Mean	Maximum	Artefacts Minimum	Artefacts Maximum
Grey level	20	20	20	20	—
Area	48 pixel ²	95 pixel ²	136 pixel ²	24 pixel ²	250 pixel ²
Horizontal diameter	8.3 pixel	—	13.26 pixel	6 pixel	—
Vertical diameter	7.42 pixel	—	11.81 pixel	6 pixel	—
Form factor	1.03	1.11	1.29	1.33	—
Grey level discontinuity	152	—	192	98	—
Width of transition zone	3 pixel	—	7 pixel	6 pixel	—
Grey level slope in transition zone	180/7 pixel ≈26/pixel	—	181/3 pixel ≈60/pixel	98/6 pixel 16/pixel	—

Table 2. Equivalent of Table 1 for Purkinje images IV

	Minimum	Maximum	Artefacts Minimum	Artefacts Maximum
Grey level	≈ 150	20	—	20
Area	9 pixel ²	12 pixel ²	—	—
Size	3 × 3 pixel ²	3 × 4 pixel ²	30 pixel ²	4 × 4 pixel ²
Diameter	1.5 pixel	3 pixel	—	—
Grey level slope in transition zone	40/pixel	165/2 pixel $\approx 80/\text{pixel}$	35/pixel	80/pixel

Table 3. Characteristics of the pupillary region

	Minimum	Mean	Maximum	Artefacts
Grey level	184	202	218	—
Area	8972 pixel ²	—	25,392 pixel ²	3000 pixel ²
Horizontal diameter	104 pixel	—	172 pixel	—
Vertical diameter	110 pixel	—	187 pixel	—

Table 4. Characteristics of the pupil boundary

	Minimum	Maximum	Artefacts
Horizontal diameter	106 pixel	174 pixel	—
Vertical diameter	111 pixel	190 pixel	—
Grey level discontinuity	130	55	98
Width of transition zone	10 pixel	16 pixel	6 pixel
Grey level slope in transition zone	55/14 pixel $\approx 4/\text{pixel}$	128/10 pixel $\approx 13/\text{pixel}$	98/6 pixel $\approx 16/\text{pixel}$

Table 5. Characteristics of the iris region

	Minimum	Mean	Maximum
Grey level	73	114	139
Horizontal diameter	252 pixel	—	322 pixel

Table 6. Characteristics of the limbus (corneal boundary)

	Minimum	Maximum	Artefacts
Horizontal diameter	258 pixel	329 pixel	—
Grey level discontinuity	39	88	98
Width of transition zone	20 pixel	30 pixel	6 pixel
Grey level slope in transition zone	43/30 pixel $\approx 1.4/\text{pixel}$	88/26 pixel $\approx 3.4/\text{pixel}$	98/6 pixel $\approx 16/\text{pixel}$

the cornea, leading to filament-like structures being imaged as specular reflections, reducing image contrast. When these structures cross somewhere in the pupil region, they may reach the brightness and size of Purkinje images IV. When these artefacts deteriorate the Purkinje reflection pattern, the algorithm should issue a warning and reject this image.

3.2. Step 2—structure of the algorithm

The algorithm was structured in six steps A–F to retrieve the required information, i.e. the coordinates of Purkinje images I and IV and the pupil and limbus centre. If Purkinje images IV could not be found, then the limbus centre had to be located in order to use the corneal (Hirschberg) technique to compute the eye alignment. If the limbal centre could not be identified, then the pupil centre should be used instead. Ambiguous results had to be identified in a final check. If necessary, *a priori* knowledge could be used by the algorithm to make a decision as to which coordinates were right. Otherwise, a warning should be issued by the program indicating that the results must be checked by the examiner.

3.3. Step A: localization of Purkinje images I in the original picture

Purkinje images I were the brightest elements of infrared pictures of the eye's anterior segment (see Figs 1–5). Their dynamics could not be represented fully due to the limited 8bit depth. Therefore, peaks always reached saturation. Their grey level was 20 (see Table 1). From the large saturated surface, the centre of gravity was calculated. A fixed grey level of 21 was chosen for thresholding.

The picture was then binarized and inverted. Through this operation Purkinje images I appeared as black dots, together with areas of the same grey level, see Fig. 7. Finally, the centres of Purkinje images I were located and their contours were fitted to circles with a standard particle analysing function implemented in the NIH image 1.57 software package [22]. From the resulting circular areas those lying within the range of Purkinje images I were selected (see Table 1). Form factors, the ratios of horizontal to vertical width, were used to differentiate further between artefacts and Purkinje images I. In case of artefacts impairing the safe detection of exactly three Purkinje image I like objects, the algorithm performed a second attempt with step C.

3.4. Step B: separation of the pupillary segment

Independently of step A, in this step, the pupillary region was identified as the region of interest where Purkinje images IV could later localized (step D). The pupil centre's initial coordinates were used for establishing the limbal centre (step E).

In histograms of the original image (see Fig. 1), the peak belonging to the pupil segment was always clearly visible at the end of the spectrum and well separated from the other grey level peaks, see Fig. 4. This histogram, with a discrete grey level distribution, was filtered with a low band pass in order to ensure a reliable thresholding just under the pupil peak. The resulting smooth function was differentiated to determine the slope and its extremes. Starting from the maximum value of the slope, that is coming from the darker grey levels, the grey level threshold value T_{pupil} was lowered until the slope reached a predefined value. This truncation value was chosen in earlier trials so that the corresponding grey level threshold was close to the peak itself, thereby eliminating pixels that did not belong to the pupil segment.

After binarization with the pupil threshold T_{pupil} , segmented areas were localized with the particle analysis function as in step A. The largest single area was the pupil segment, see Fig. 6, from which the centre of gravity was determined.

3.5. Step C: localisation of Purkinje images I

In this step, designed as alternative to step A, Purkinje images I were detected based on the high contrast against the pupil ROI. The grey level profile through Purkinje images I in Fig. 5a illustrates the large grey level difference between the pupil ROI and the segments

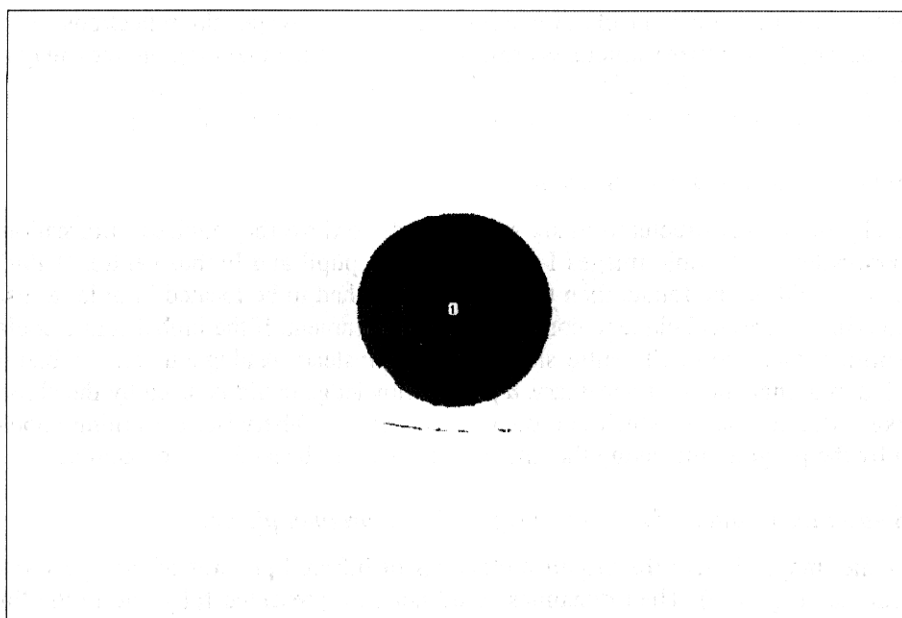


Fig. 6. Identification of the pupil region with binary threshold derived from histogram, Fig. 4. The number (1) designates the centre of the limbus and of the pupil that coincided in this example. The interrupted curved black line beneath is a reflection artefact from the meniscus of the tear film.

belonging to Purkinje images I. In order to detect these edges the grey level profile was differentiated line by line in the ROI. If a positive threshold value for the slope was exceeded in a pixel, then this pixel and the next two in the same line were given the maximum grey level (255). In this way the rising slope is marked. On continuing, the pixel would be marked where the slope reached or exceeded the same, now negative, value. Next, the corresponding pixel and the two preceding ones were marked with maximum grey level 255. Any pixel falling between the upper and lower limits for the slope was given the grey level 0, i.e. white. When this was done line by line Purkinje images I appeared as circles on a uniform background. Then a dilation was performed so that small circles stemming from Purkinje images I would be filled completely, while larger structures would remain hollow. This allowed a particle identification algorithm to be used to differentiate between the filled and hollow structures. Separation of the edges of Purkinje images I could also be done with a 3×3 Sobel-kernel [24] followed by a binarization. However, this would have been more time consuming than the procedure described above. Figure 7 shows the marked Purkinje images I as disks whose diameter range was known, while sharp edges stemming from large spectacle artefacts could not form closed structures of the same size. Moreover, their form factor was different from that of the Purkinje images. With this information Purkinje images I were reliably separated from other structures and artefacts that reached saturation level.

3.6. Step D: localization of Purkinje images IV in the pupil ROI

The area inside the pupil contour found in step B was taken as ROI. Figure 5b shows that Purkinje images were usually well above the pupillary noise level. However, artefacts may be of the same height and similar size. The images were separated from the pupil with a threshold derived in a similar way as the threshold T_{pupil} gained from the histogram Fig. 4 in step B.

Here the optimized choice of T_{pupil} was crucial so that all Purkinje images IV would be included, without reducing their surface, but a number of artefacts could be selected in the procedure. Therefore, a particle identification algorithm was used and the sizes and form factors were compared to the known ranges for those structures to distinguish artefacts from Purkinje images IV. This algorithm worked well provided the images were well exposed,

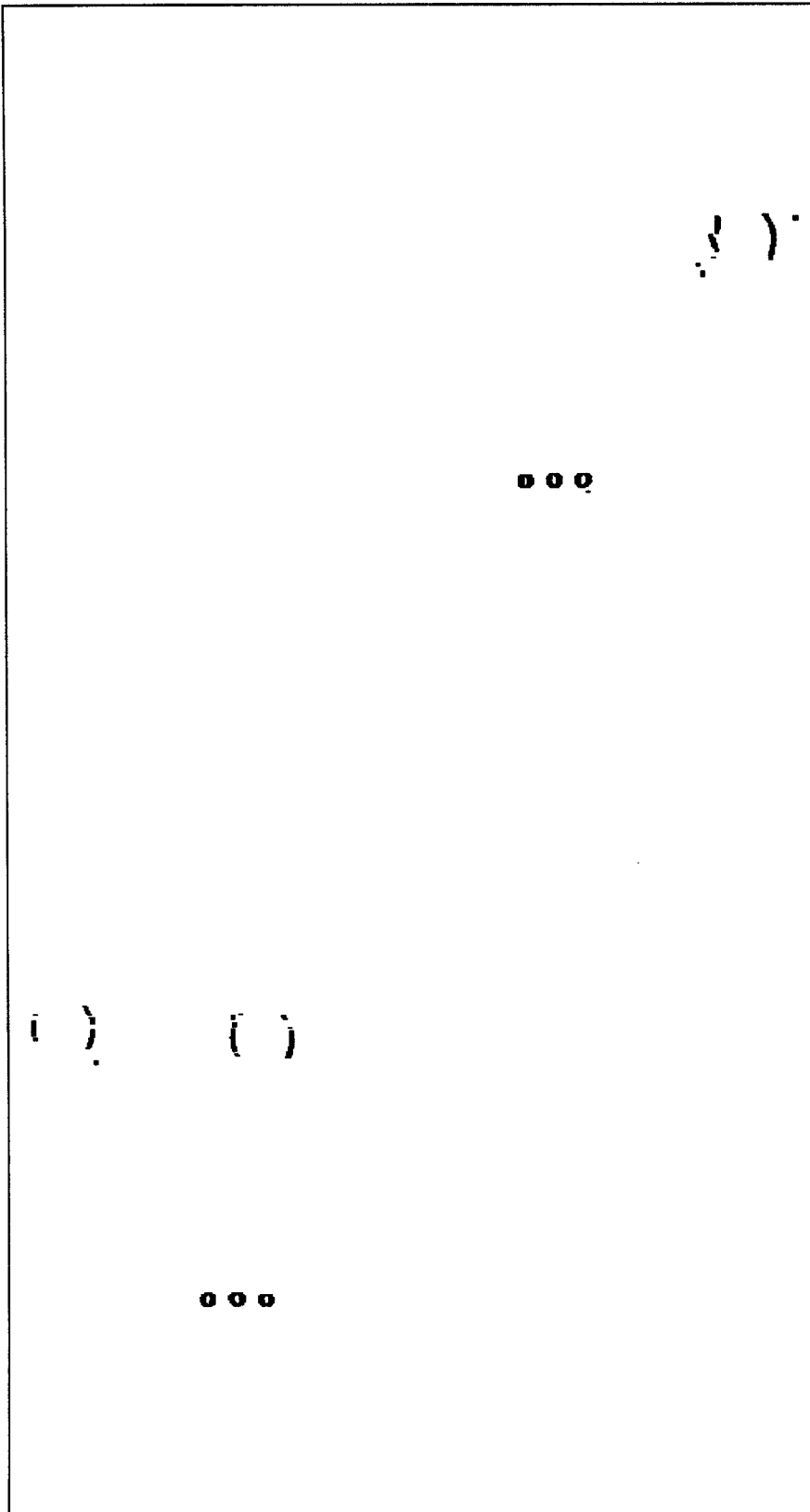


Fig. 7. Separation of Purkinje images I from larger areas of same brightness by image processing step C. The processing results in a binarization with closed borders of the three Purkinje images I, while the borders of spectacle artefacts are not closed. The closed structures are then extracted with a particle algorithm tuned to the ranges of diameters and form factors of Purkinje images I.

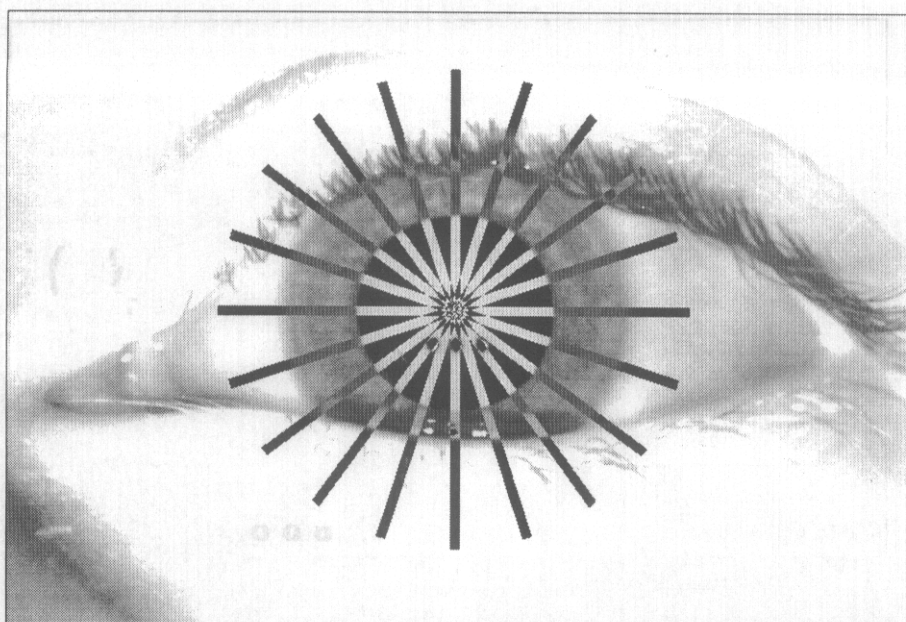


Fig. 8. Identification of the limbus boundary with radially oriented ROIs. The grey scale is inverted in the ROIs for better visibility. Differentiation along the ROIs yields the slope's maxima, thereby identifying the pupil and limbus boundary. Due to the position of the eyelids, the boundaries of the limbus are usually not visible all around the clock. Only regions with a transition towards white (sclera), that is nasally and temporally, are admitted in the subsequent evaluation.

i.e. the contrast between the pupil segment and Purkinje images IV was sufficient. However, Purkinje images could be visible with the naked eye, but still hidden by artefacts.

If not enough Purkinje image IV like structures were found with the histogram-based method described above, then local grey level extremes were calculated in the pupil ROI by two-dimensional differentiation and subject to the same checks as above.

3.7. Step E: radial strip ROI algorithm for the detection of the boundaries of the pupil segment and the limbus

3.7.1. *Part 1: radial strip ROI.* Radial strip ROIs were constructed starting from the centre of the pupil segment, see Fig. 8. Their width was 8 pixels. Their length was determined by the largest expected diameter of the iris, which was part of the *a priori* knowledge. Grey levels were averaged normally to the radial strip ROI to minimize noise and artefact interference. Then the one-dimensional grey level profile was smoothed by filtering with a 5*1 low pass filter. This was done to ensure that the gradient could not be biased by local artefacts. The radial strip ROI intersected the pupil boundaries and the limbus almost normally. Therefore the grey level transition zones corresponding to these structures were narrow, and the slopes were steep (see Fig. 9). Since the grey level transitions went from darker (high grey levels) to lighter image portions (low grey levels), the slopes were negative.

3.7.2. *Part 2: detection of the pupil boundary.* The range of pupil diameters or pupil radii is known as *a priori* knowledge. Therefore, local minima of the slope were sought that fell within this range. These belonged to the pupil. Their coordinates were stored and the corresponding image elements were marked for display with "P"s in Fig. 10. These coordinates were used in step F to fit ellipses to the pupil.

3.7.3. *Part 3: detection of the limbus.* The iris showed considerable variations of grey level and therefore several local minima could be found in the grey level profiles of the radial strip ROI in the iris region (see Fig. 9). Therefore, the **smallest** minimum was selected by the algorithm and marked with an "L" indicating the limbus (see Fig. 10). Usually, eyelids and eyelashes covered large portions of the upper and lower limbus.

Consequently, only the lateral limbus sectors were recruited for the limbus detection. Limbus edge markings and coordinates were, therefore, only accepted by the algorithm if they lay within the marked sectors of Fig. 10.

Occasionally, the pupil was covered by an eyelash in its upper portion, which entailed an enlargement of the pupil ROI, and a shift of the ROI's centre. This meant that the point from which the radial strip ROI was traced out to the limbus would be more eccentric, and the known range of distances of the pupil centre to the iris margin and to the limbus did no

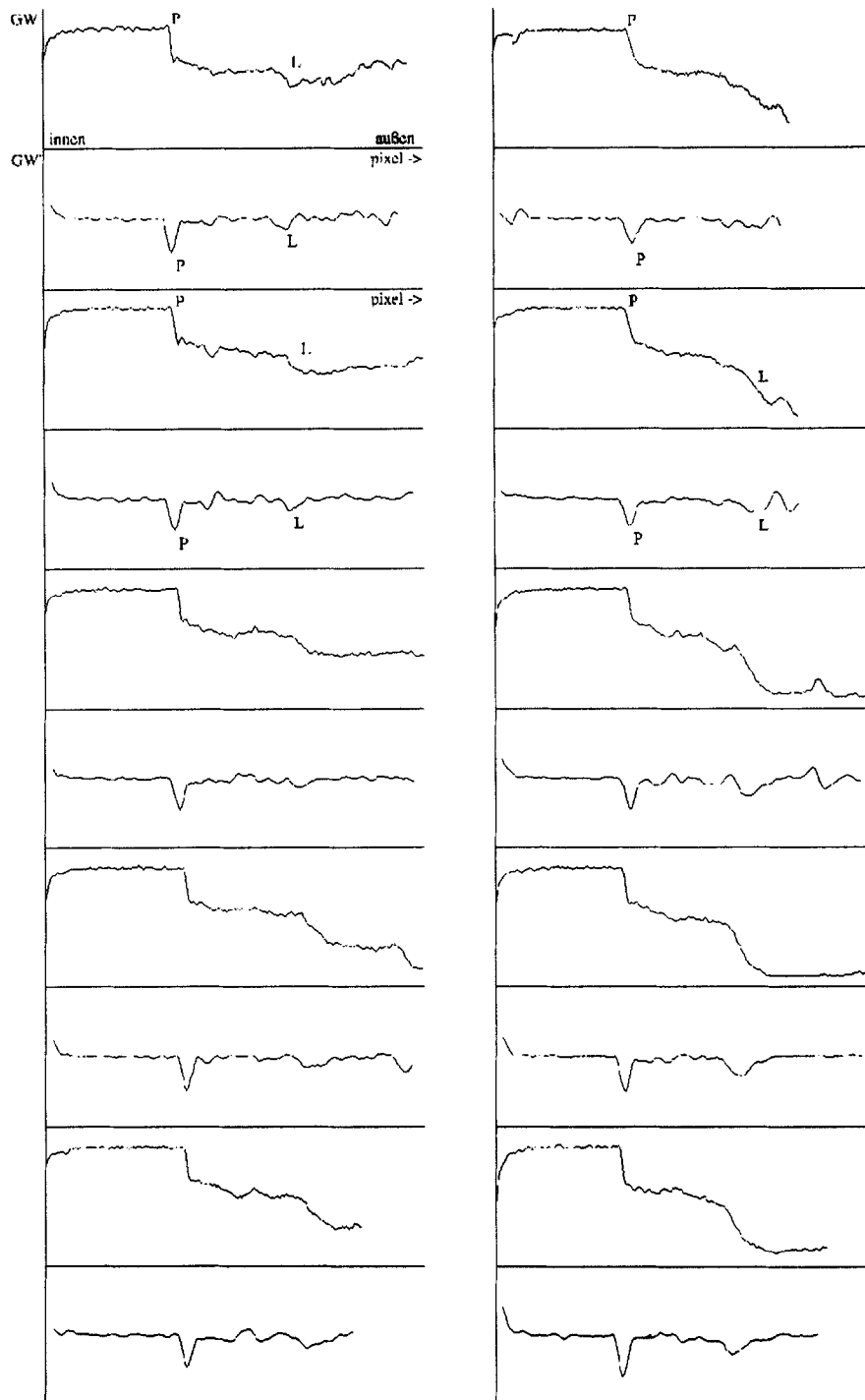


Fig. 9. Plot of strip-ROI profiles and their first order derivative (beneath) from Fig. 8. Pupil borders are marked with a "P", and limbus borders are marked with an "L" in some of the plots.

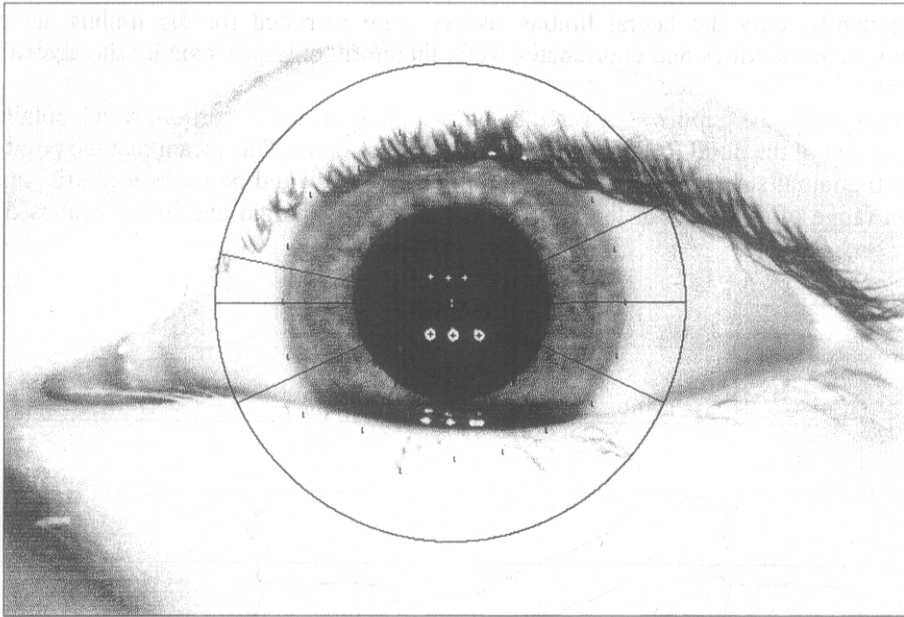


Fig. 10. Original image (see Fig. 1) with detected and marked structures after image processing with steps A to F. Purkinje images IV are marked with a white "+", and Purkinje images I are marked with a black "+", pupil borders with "P", and limbus with "L". Since the detection of the limbus will only yield reliable results in the nasal and temporal sectors where the limbus is not usually covered by eyelids and eyelashes, only the marked limbus coordinates with the left and right sectors are used in further calculations.

longer apply. This effect could be balanced by allowing pupil and limbus radius ranges to vary, so that a 10% of pupil diameter shift of the ROI centre can be tolerated without negative effects.

3.8. Step F: determination of pupil and limbus centres and diameters

The acquired coordinates of points on the pupil border and on the limbus were used to fit circles (limbus) and ellipses (pupil). The centres and radii of these were needed for the measurement of the ocular alignment with corneal reflexes alone. The tentative centre of the pupil ROI from step B was used as an initial value for the pupil and limbus centre. The fitting procedures were based on iterative algorithms and on least squares optimization [25].

As part of the consistency check, individual points whose squared distance from the fitted circles and ellipses exceeded a threshold were excluded from the data, and a new circle or ellipse fit was performed to find the centre and diameter of the limbus and pupil.

3.9. Consistency check

The final results (positions of Purkinje images I and IV, pupil and limbus centre positions) were compared to *a priori* knowledge that was not used in the processing of the images. For instance, there must be three Purkinje images I and IV, the Purkinje images I and IV must lie on two horizontal lines, and their relative distances must match the known ranges. Also, to ensure diagnostic safety, Purkinje images IV should not be closer to Purkinje images I than a certain known distance given by the light source set up, and so on.

Unless the image processing ended without any inconsistencies, the examiner received a warning asking for a check and an interactive correction or completion of the image evaluation.

In step 3, the algorithm was implemented as Pascal code (Turbo Pascal 6.0, Borland, Scotts Valley, CA, U.S.A.).

4. RESULTS AND DISCUSSION

Typical execution time for one image was less than 500 ms. This meant that the result of the evaluation of a Purkinje image I and IV reflection pattern of a right and a left eye was available immediately after each image taken, and pictures with erroneous fixation could be discarded immediately. This improvement is essential for the clinical application of the ocular alignment method in a screening device since imperfect images may now be repeated immediately in order to obtain a complete image data set within the limited attention span of toddlers and infants.

To investigate the reliability and flexibility of the algorithm, a new batch of test images with different image characteristics was obtained from 30 subjects recruited at random in the outpatient department of the university eye clinic and from eye clinic staff. The age of the subjects ranged from 6 to 55 yr of age, with dark and light irises. Both right and left eyes were recorded, without glasses. Nine different gaze directions were recorded to simulate a wide range of possible misalignments and to obtain many differently structured Purkinje reflection patterns.

To make image analysis more difficult, the image format was increased, so that image resolution dropped by a third compared to the original laboratory images. As imaging devices, a different pair of CCD cameras (505, GBC Ltd., Welwyn, U.K.) was used, in the interlace mode, at a shutter speed of 1/50 s, with automatic gain. Therefore, the half images were often slightly shifted relative to one another by a pixel due to object motion, thereby reducing image contrast.

After adjusting the algorithm's parameters to the new image data, the algorithm was tested on the new image database (540 images). All images were either correctly interpreted, or a warning was issued (approximately 10% of eyes). Typical reasons for rejection were: overlapping of hair over Purkinje reflection patterns, beginning lens opacification in subjects over 40–50 yr of age, reduced contrast in the image, probably due to the automatic gain.

This means that all technically imperfect images were correctly identified, and images with gaze directions where Purkinje images I and IV were too close to allow a safe evaluation were evaluated with the alternative corneal reflex approach. At the same time, pathological conditions of the eye like ptosis, corneal or lens opacities and others result in atypical images, which cannot be evaluated automatically. In these cases the warning issued by the program can contain a hint regarding this risk factor, leading to referral of the subject.

Using the information on pupil and limbus diameter, additional screening criteria can be implemented, since the limbus diameter indicates juvenile glaucoma, and pupil diameter anomalies indicate neuro-ophthalmological disorders. Finally, Purkinje image I distances calculated from corneal reflex coordinates can be used to compute corneal power and astigmatism, both important screening data [26]. This opens the way for accurate, cost-effective, automated use of Purkinje I and IV reflection pattern evaluation and other examinations in vision screening devices.

The current program version may further be optimized for speed, in a more powerful programming language. Due to the simplicity of the algorithm that consistently avoided time consuming operations, optional real time processing with 5–10 Hz seems feasible with current hardware, i.e. Purkinje I and IV eye tracking could be achieved. This option may be of interest since the *dynamics* of eye movements offer additional clues in the detection of ocular misalignment and with respect to other applications requiring accurate remote ocular alignment monitoring under natural, binocular viewing conditions.

5. SUMMARY

Microtropia is a cosmetically inconspicuous form of strabismus with small angles of strabismus up to 5°. If not detected and treated within the first years of life, this condition, which affects about 1% of subjects in Western Europe, leads to irreversible loss of vision in the affected, misaligned eye (amblyopia).

Purkinje images are specular reflections of light sources in the eye, the position of which is proportional to eye rotation. Corneal reflex techniques have long been used for ocular alignment assessment and eye tracking in medicine and research. These clinically well established techniques, however, are not accurate enough for detection of microtropia.

More accurate screening techniques for ocular misalignment use the posterior crystalline lens reflex (Purkinje image IV) and the limbus center in addition to the anterior corneal reflex and the pupil center. For standard corneal reflex techniques, clinically useful image processing algorithms were described by many researchers. They are not suited to detect the crystalline lens reflections nor the limbus, that is the boundary between the sclera and the iris, since these image elements have varying, low contrast.

Therefore, the purpose of this study was to develop a fast and reliable image processing algorithm for the extraction of Purkinje image I and IV data from images of the anterior eye segment for measurement of ocular alignment and misalignment in ophthalmology with standard PC hardware.

Preliminary tests revealed that image contrast was better with infrared light than with visible light. Three near infrared emitting light diodes were used to generate Purkinje I and IV reflection patterns which were recorded in each eye with two CCD cameras. Image data consisted of b/w digitized images (768×512 pixel², 8 bit depth) of right and left eyes, each showing three Purkinje I and three Purkinje IV images and the anterior eye segment.

In the first step, a thorough descriptive analysis of a set of images was done prior to developing a strategy for localization of Purkinje images I and IV, the pupil centre and the limbus centre. In the second step, an algorithm was designed with standard software modules and histogram-based thresholding and gradient techniques using a macro-programming language. Adjustable evaluation parameters accounted for different signal characteristics of images from different recording devices. In the third step, the algorithm was implemented in a higher programming language. Typical execution time was less than 500 ms per image. Final image processing results were checked for consistency by the algorithm to ensure diagnostic safety.

A set of 540 images with reduced resolution from a different set of CCD cameras from 30 subjects which included various artefacts and different gaze directions. Ninety-four percent of the images were automatically and correctly analysed. The rest was rejected because they could not be evaluated at all, or because they required interactive completion of the evaluation or processing with more time-consuming algorithms. With this fast algorithm, automatic evaluation of a set of 20 images, as required for screening applications, is achieved in less than 10 s. This will allow for implementation of more accurate objective ocular alignment screening techniques into cost-effective automated ophthalmological screening devices, along with use of Purkinje I and IV reflection pattern evaluation for other purposes which require high accuracy and natural viewing conditions.

Acknowledgements—This work was supported by Deutsche Forschungsgemeinschaft grant # Ef 6/3-2 and Ba 1316/5-3. Corporate support from Adatomed Intraocular Lenses, Munich, Germany, from National Instruments, Munich, Germany, from MIT, Aachen-Kornelimünster, Germany, and from Graftek, Mirmande, France is gratefully acknowledged.

REFERENCES

1. H. Kaufmann, W. de Decker, D. Friedburg, W. Haase, G. Kommerell and W. Rüßmann, *Strabismus*, pp. 202–279. Enke, Stuttgart (1986).
2. G.K. von Noorden, *Binocular Vision and Ocular Motility*, 4th ed., pp. 208–245. C.B. Mosby, St Louis (1990).
3. A. Fulton, Screening preschool children to detect visual and ocular disorders, *Arch. Ophthalmol.*, **110**, 1553–1554 (1992).
4. R.D. Reinecke, Screening 3-year olds for visual problems, *Arch. Ophthalmol.*, **104**, 33 (1986).
5. A. Hohmann and W. Haase, Effektives Seh-Screening kann Amblyopierate senken, *Ophthalmologe*, **90**, 2–5 (1993).
6. J.C. Barry, R. Effert, A. Kaupp, M. Kleine and M. Reim, Computergestützte Messung von Augenfehlstellungen bei Säuglingen und Kleinkindern mit Hilfe des digitalen Purkinje Reflexmusterverfahrens, *Der Ophthalmologe*, **91**, 51–61 (1994).
7. A.G. Bennett and R.B. Rabbetts, *Clinical Visual Optics*, 2nd ed., pp. 261–264. Butterworths, London (1989).
8. J.E. Purkinje, *Commentatio de Examine Physiologico Organi Visus*, pp. 1–58. Junk, Breslau (1823).

9. R. Jones and J.B. Eskridge, The Hirschberg-Test—a re-evaluation, *Am. J. Optom.*, **23**, 105–114 (1970).
10. S.E. Brodie, Photographic calibration of the Hirschberg test, *Inv. Ophthalm. Vis. Sci.*, **28**, 736–742 (1987).
11. P.M. Riddell, L. Hainline and I. Abramov, Calibration of the Hirschberg test in human infants, *Inv. Ophthalmol. Vis. Sci.*, **35**, 538–543 (1994).
12. J.M. Miller, M. Mellinger, J. Greivenkamp and K. Simons, Videographic Hirschberg measurement of simulated strabismic deviations, *Invest. Ophthalmol. Vis. Sci.*, **34**, 3220–3229 (1993).
13. F. Schaeffel, H. Wilhelm and H. Zrenner, Inter-individual variability in the dynamics of natural accommodation in humans: relation to age and refractive errors, *J. Physiol.*, **461**, 301–320 (1993).
14. J.R. Charlier, M. Behague and C. Buquet, Shift of the pupil center with constriction, *Inv. Ophthalm. Vis. Sci.*, **35**, S1278 (1994).
15. H.J. Wyatt, The form of the human pupil, *Vis. Res.*, **35**, 202–2036 (1995).
16. J.C. Barry, R. Effert and A. Kaupp, Objective measurement of small angles of strabismus in infants and children with photographic Purkinje reflection pattern evaluation, *Ophthalmol.*, **99**, 320–328 (1992).
17. J.C. Barry, R. Effert, A. Kaupp and A. Burhoff, Measurement of ocular alignment with photographic Purkinje I and IV reflection pattern evaluation, *Inv. Ophthalmol. Vis. Sci.*, **35**, 4219–4235 (1994).
18. J.C. Barry, R. Effert, M. Reim and D. Meyer-Ebrecht, Computational principles in Purkinje I and IV reflection pattern evaluation for the assessment of ocular alignment, *Inv. Ophthalmol. Vis. Sci.*, **35**, 4205–4218 (1994).
19. J.C. Barry, R. Effert and N. Hoffmann, Nachweis und Diagnose von kleinen Augenfehlstellungen mit dem Purkinje-Reflexmusterverfahren, *Klin. Monatsbl. Augenheilkunde*, **208**, 167–180 (1996).
20. T. Lehmann, A. Kaupp, R. Effert and D. Meyer-Ebrecht, Automatic strabometry by Hough-transformation and covariance-filtering. In *Proceedings of the ICIP-94, Austin, TX*, IEEE Computer Society Press, pp. 421–425 (1994).
21. International Electrical Committee, *IEC 825-1 Safety of Laser products—Part 1: Equipment classification, requirements, and users's guide*. VDE Verlag, Berlin (1993).
22. W. Rasband, *NIH Image 1.57 Manual*. National Institutes of Health, Bethesda, MD (1995).
23. M.C.M. Dunne, J.C. Barry, A. Hartmann, F. Culpin, L. Demain, A. Duke and I. French, Measurement of corneal and crystalline lens misalignment relative to the visual axis, *Vis. Res.*, **35**, S199 (1995).
24. B. Jähne, *Digital Image Processing: Concepts, Algorithms, and Scientific Applications*, 3rd ed., pp. 146–147. Springer, Heidelberg (1996).
25. I.N. Bronstein and K.A. Semendjajew, *Taschenbuch der Mathematik*, pp. 782–833. Hard Deutsch, Leipzig (1979).
26. J.M. Miller, M.D. Mellinger and J.E. Greivenkamp, A hand-held video keratoscope for the measurement of corneal astigmatism in infants and young children. In *Vision Sciences and Its Applications, OSA Technical Digest Series (Optical Society of America, Washington DC)*. Technical Digest Series 1996, Vol. 1, pp. 260–264 (1996).

About the Author—J.C. BARRY was born in Vietnam in 1959. He received the MSc in physics in 1987 from RWTH University in Aachen, Germany, the MD degree in 1990, and the PhD in 1991 from the same university. He passed the board exam in ophthalmology in 1997. Part of his training/experience was acquired in France, Switzerland, Spain, and the U.S.

Fields of interest and research include physiologic optics, objective strabismus diagnosis, visual impairment screening methods, image processing techniques, ray trace algorithms, and medical data classification algorithms. In this field several patent applications have been filed.

His research projects have been funded both by faculty grants and national grants, and a number of international and national collaborations contributed to the success of these projects. He has authored more than 10 research papers in international journals.

Currently, J.C. Barry is heading an interdisciplinary research team at RWTH Aachen University, and is involved with student training. He supervised the degrees of more than 15 medical, engineering, and physics postgraduates. The *leitmotiv* of his research has been that, to strengthen medical science and practice, objective reproducible techniques developed with mathematical and engineering tools are essential.

About the Author—UWE M. PONGS was born in Moenchengladbach-Rheydt, Germany in 1966 and studied Biomedical Engineering with a focus on medical informatics and medical image processing. He obtained the diploma in Biomedical Engineering from the FH Aachen/Jülich University, Germany in 1995. The present work summarizes his thesis which was conducted in the Research Group for Physiologic Optics and Strabismus Diagnosis of the RWTH University Eye Clinic, Aachen, Germany.

In 1986, he founded a company for the development of industrial measuring soft- and hardware. Since 1994 he has focused on measuring techniques in vision science, medical and industrial image processing and industrial visual measuring methods which led to his present activities, the technical development of ophthalmological measuring devices.

About the Author—WALTER HILLEN studied Mathematics and Physics at the University of Bonn, Germany and received the MS degree in 1977. After receiving the PhD in 1981 he worked in high energy physics at the storage ring DESY, Hamburg. In 1983 he joined the Philips Research Laboratory, Aachen and worked in the area of digital radiography.

Since 1992 he has been a Professor of Medical Computer Science and Engineering at FH Aachen/Jülich University, Germany. His current research interests are in medical image processing, machine vision and multimedia information systems.